doi: 10.82124/CEAS-GNC-2026-109 CEAS-GNC-2026-109

Aeroelastic Flight Control Validation in a Simulation-Enhanced Wind Tunnel Experiment

Felix Stalla Research Associate, German Aerospace Center (DLR), Institute of Aeroelasticity, Weßling, Germany. felix.stalla@dlr.de
Ph.D. Student, Delft University of Technology (TU Delft), Delft, The Netherlands.

Gertjan Looye Head of Department, German Aerospace Center (DLR), Institute of Aerelasticity, Weßling, Germany. gertjan.looye@dlr.de

Thiemo M. Kier Head of Group, German Aerospace Center (DLR), Institute of Aerelasticity, Weßling, Germany. thiemo.kier@dlr.de

ABSTRACT

For novel passenger aircraft with pronounced aeroelastic effects, primary flight and aeroelastic control should be addressed simultaneously, and, due to their inherent coupling with the airframe, flight control development should begin early in the aircraft's design process. To facilitate such a control co-design, early stage, cost-effective hardware tests are required, to validate and mature the developed controllers. Wind tunnel testing provides hardware-in-the-loop capabilities to test primary flight and aeroelastic control. However, it poses constraints on model size and realizable maneuvers. To address these challenges, this paper proposes a simulation-enhanced wind tunnel testing approach, in which the physical model is augmented by an aircraft simulation. The setup is tailored to aeroelastic applications by testing only a subcomponent of the aircraft, typically the wing, inside the wind tunnel, while representing the remaining aircraft dynamics in simulation. This allows the component to be scaled for best representation of the aeroelastic behavior. This paper presents the overall architecture of this setup, including the interfaces between experiment and simulation, and the implementation of the control functions to be validated. The capabilities of the approach are demonstrated by the implementation and experimental validation of an integrated control design combining primary flight and aeroelastic control. A roll rate-command attitude-hold controller is coupled with gust load alleviation. The validation allows to assess the performance of the control law and the interaction between primary flight and aeroelastic control. The results demonstrates the merit of such a simulation-enhanced wind tunnel test in controller development, allowing for a cost-effective wider range of testing scenarios.

Keywords: Wind Tunnel Testing, Flight Control, Aeroelastic Control, Validation & Verification

1 Introduction

Aeroelastic effects become increasingly important in the design of modern passenger aircraft, giving rise to the development of secondary flight control functions that address these aeroelastic effects [1, 2]. Most of these secondary functions aim to adapt the dynamic response of the flexible aircraft [3], to reduce the occurring loads and thus reduce the structural weight of the aircraft [4]. To maximize the potential for structural weight savings, control design must be integrated into the earliest stages of the aircraft

development cycle, ideally already during preliminary design [1]. Also, the design of secondary control functions needs to be closely coordinated with primary flight control (PFC) design, since rigid-body and flexible dynamics interact, and all control objectives and available bandwidth needs to be balanced [5, 6]. This suggests a control co-design [7], in which control development is performed alongside all the other disciplines of aircraft development, such as structures, aerodynamics, or propulsion.

For an effective control co-design, it is important to validate control concepts early on, in a fast, iterative fashion, to mitigate the risk. To validate flight control concepts augmented by aeroelastic functions, several techniques are available. Moving from low to high effort and cost, examples in literature on flexible aircraft flight control contain: numerical simulations [8], hardware-in-the-loop (HIL) tests on a test bench [9], wind tunnel tests [10, 11], sub-scale flight tests on a UAV (unmanned aerial vehicle) [12, 13], and full-scale flight tests on actual aircraft [14, 15]. As aerodynamics present a major source of uncertainty, it would be advantageous to use validation approaches like wind tunnel or flight tests that capture aerodynamic effects physically and not to rely on simulation only. Given the limited availability of flight test platforms, especially for combined primary and aeroelastic control validation, wind tunnel tests offer a suitable compromise, and are the focus of this paper.

Several methods have been proposed for validating PFC laws in wind tunnels, as reviewed in [16]. This approach has been introduced as so-called virtual flight testing [17, 18], to bridge the gap between ground and flight testing. In the field of aeroelasticity, wind tunnel tests historically played a fundamental role in the development process from the very beginning [19]. Testing in a wind tunnel has the advantage of being cost-effective, allows to install a substantial amount of measurement equipment, provides a safe environment, and offers controlled and reproducible testing conditions [20]. Reproducible conditions are especially useful for aeroelastic control functions such as gust load alleviation (GLA), when the same gust can be imposed repeatedly onto the aircraft while the controller is switched on and off [21]. In atmospheric flight conditions a repeated gust encounter is difficult to realize. The wind tunnel environment also allows for a low-risk testing of experimental controllers, since the experiment can be stopped instantaneously [22].

However, also wind tunnels experiments include a number of constraints. There are limitations in size, so the aircraft under test is typically downsized to match the wind tunnel dimensions, leading to the use of similarity conditions [20, 23]. Matching all similarity conditions in aeroelastic tests is hard to achieve. Especially due to limited model size it is difficult to match the flexible eigenfrequencies of the aircraft, such that these are usually higher then for a full-scale aircraft [24]. For flight control tests, a second important constraint is the attachment of the aircraft in the wind tunnel. This limits the motion of the aircraft in space, thus confines the testable maneuvers and the available measurement signals. There have been experiments with free-flying aircraft in the wind tunnel, where the model is only attached to a cable to convey the measurement signals and to add safety to the test [25]. This approach has even been applied for aeroelastic control validation [22, 26] but most wind tunnel tests are still conducted with the the model being mounted to a sting or a balance. In such a setup, objectives and test procedures must be adapted to cope with the constraints of the wind tunnel setup.

To address above mentioned limitations, this paper presents a simulation-enhanced wind tunnel test approach for validation of aeroelastic control functions integrated with PFC. In this setup, only a component of the aircraft (e.g. wing, empennage, or half model) is physically tested in the tunnel, feeding information to a controller executed on a real-time system, while a simulation model completes the closed-loop system by supplying the remaining flight dynamics. This approach enables direct capture of aerodynamic effects, which are often the largest source of uncertainty in control law validation, particularly under unsteady and nonlinear flow conditions, while maintaining a safe, controlled, and reproducible testing environment. Focusing on a single component allows increased geometric scaling, leading to favorable aeroelastic properties such as lower flexible eigenfrequencies. These are essential to ensure that the sensing and actuation system can achieve sufficient bandwidth to address the frequency

ranges of interest. In addition, the larger model scale facilitates integration of sensors and actuators. A similar concept has been proposed in [27], where rigid-body dynamics in response to a gust are represented by imposing a pitch and plunge motion on a wing model. In contrast, the present paper is focused on control law validation.

The approach of a simulation-enhanced wind tunnel experiment is used to validate an integrated primary flight and aeroelastic control law. It acts as a rate-command, attitude-hold controller (RCAH) for the roll axis, while simultaneously reducing gust and turbulence disturbances. The integrated inner-loop for reference tracking of roll acceleration and gust load alleviation introduced in [28] is now combined with a RCAH outer-loop to complete the primary flight control functionality.

Section 2 introduces the simulation-enhanced wind tunnel testing concept, detailing the interconnection of a model in the wind tunnel, a numeric simulation model running in parallel, and a controller executed on real-time hardware. The framework's application to the integrated roll RCAH and GLA controller follows: Section 3 describes the application case and defines control objectives, Section 4 outlines the aeroelastic modeling for simulation and control design, Section 5 details the control synthesis, and Section 6 contains the experimental results from the German-Dutch low speed wind tunnel in Braunschweig (DNW-NWB). The application case illustrates the formulation of equivalent control objectives, measurements, and control actions to mitigate wind tunnel limitations, demonstrating the framework's ability to assess controller performance and primary-secondary flight control interactions.

2 Concept of Simulation-Enhanced Wind Tunnel Testing

To validate control algorithms, the controller is interconnected with the plant to form a closed-loop system, whose properties can then be analyzed. This validation typically progresses from software-in-the-loop (SIL), where all components are simulated, to hardware-in-the-loop (HIL), where the controller runs on real-time hardware connected to all or parts of the aircraft existing as (scaled) hardware. For flight controllers, particularly those facing complex aerodynamics, wind tunnels offer a high-fidelity HIL environment. However, wind tunnel models are inherently limited by physical constraints on flight dynamics, propulsion, and atmospheric conditions. To overcome these, several concepts reviewed in [16] propose a wind tunnel based virtual flight test. This hybrid approach operates the wind tunnel hardware (HIL) in parallel with an aircraft simulation (SIL). Both components are interconnected with the controller by (virtual) sensors and (virtual) actuators. The controller is hosted on a real-time system, that also runs the aircraft simulation. Wind-tunnel hardware and aircraft simulation can exchange information.

In contrast to the concepts reviewed in [16], the simulation-enhanced HIL setup proposed here is specifically tailored to aeroelastic control functions integrated with primary flight control. To accurately replicate aeroelastic properties in wind tunnel experiments, flexible models are ideally manufactured at a large scale. Due to material and manufacturing constraints, properties such as flexible eigenfrequencies scale inversely with model size, smaller models lead to higher eigenfrequencies. Therefore, this paper proposes a simulation-enhanced wind tunnel setup shown in Fig. 1, where only a component of the aircraft is placed inside the tunnel, such as the right wing. Depending on the component of interest, this could also be an aeroelastic empennage, or a wing-fuselage-tail half model. By isolating an aircraft component, the scale can be maximized to achieve manageable aeroelastic properties. While [27] explores a similar concept for aeroelastic testing, the present work focuses on simultaneous validation of primary and secondary flight control laws. Here, the physical wind tunnel model is equipped with hardware sensors and actuators, which are augmented by virtual sensors and actuators from a real-time aircraft simulation, interconnected with the controller executed on a real-time system. To validate control laws, a pilot interface is added, to inject control commands and visualize information of the aircraft simulation or wind tunnel model. The control commands can be defined using the PC interface of the real-time system, or using a pilot stick. This allows to virtually fly the aircraft in the simulation-enhanced HIL setup.

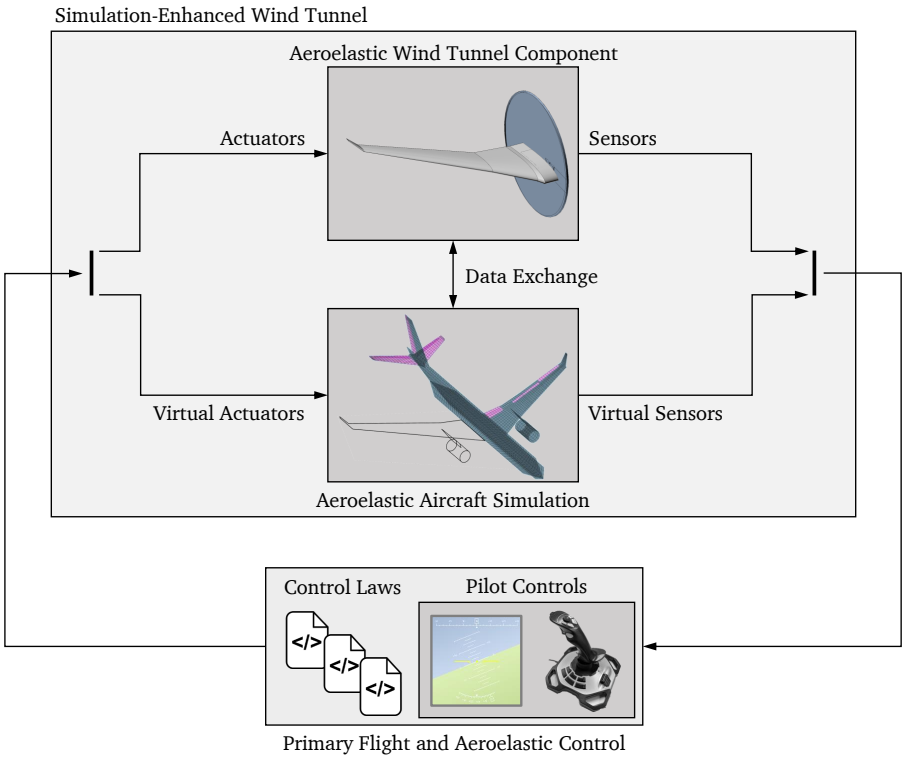

Fig. 1 Schematic depiction of the simulation-enhanced wind tunnel test.

To visualize the conceived interconnection of the three main components (wind tunnel model, aircraft simulation, controller), Fig. 2 depicts the signal flow between those components. The wind tunnel domain consists of the scaled aeroelastic aircraft component (here: wing) in the wind tunnel, including actuators (to power control surfaces such as flaps, ailerons, spoilers, etc.) and sensors (accelerometers, gyroscopes, pressure sensors, etc.). The wind tunnel model is typically mounted on a model motion system, that allows to change the orientation of the model. For aeroelastic functions such as load alleviation, a gust generator will be mounted in the tunnel, to induce atmospheric disturbances onto the model. The conditions of the wind tunnel such as flow velocity can be adapted within the feasible range. The wind tunnel may also provide additional sensors, such as a force and moment balance at the root of the model. All sensor data from the tunnel is captured by a data acquisition system.

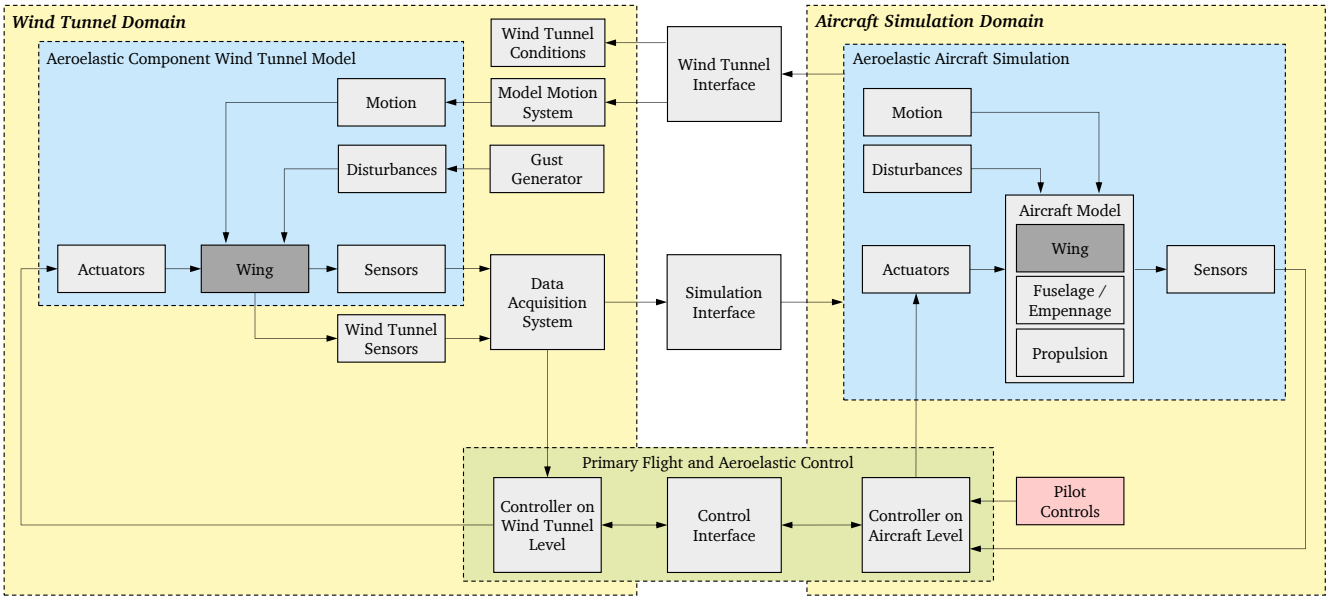

Fig. 2 Signal flow diagram between wind tunnel domain, aircraft simulation domain, and controller.

The aircraft simulation domain consists mainly of said simulation. The idea is that the simulation mirrors the experiment, however taking the full-sized aircraft with all its components into account. Obviously, depending on the desired test, the fidelity of the simulation can be reduced, from a full nonlinear aircraft to a simplified dynamic about one specific aircraft motion.

Wind tunnel and aircraft simulation domain exchange information through two interfaces. Since wind tunnel model and aircraft simulation have different scales, an important task of the interfaces is to scale the signals accordingly. Scaling of course involves much more than simple geometric scaling. An overview of similarity conditions important in wind tunnel experiments is given in [20]. It is expected that not all similarity conditions are met. Therefore, the designers shall focus on the conditions most important for control validation. The simulation interface obtains the information of the data acquisition system of the wind tunnel, scales it to aircraft level, and passes it into the simulation. There, the data is picked up and provides information for the respective aircraft component. The wind tunnel interface receives information from the aircraft simulation, and influences the wind tunnel experiment. For example, wind tunnel conditions and model orientation may be influenced by the simulation. Thereby, also the motion of the aircraft can be represented in the wind tunnel, such as the angle of attack of the wing. The wind tunnel interface also scales the received data, to be consistent with the simulation interface.

The controller executed on a real-time system operates in both wind tunnel and aircraft simulation domain. There are certain control functions that are executed on aircraft level, and others that operate on wind tunnel level. The former receive virtual sensor information from the simulation, and command virtual actuators, while the latter use sensors and actuators in the experiment. The controllers communicate through a control interface. This interface is again responsible for scaling between the domains, and this time also offers bi-directional information exchange, depending on the implemented control function.

The interfaces between the two domains, especially the controller interface, need to serve another purpose that results from placing only a component in the wind tunnel: signal emulation. Depending on the mounting of the model in the wind tunnel, it might not be possible to receive all required sensor information from the wind tunnel model that are required to perform the control task. This can be overcome by emulating the required signal, using or combining available sensor and virtual sensor information. How such a signal emulation can be realized will be discussed in the following section.

Lastly, the wind tunnel controller test is monitored and executed from a host computer, that is linked to the data acquisition system and the real-time system running the controller. This host computer is not depicted in Fig. 2. The host computer is responsible for interaction with the controller, such as enabling or disabling the controller or certain actuators, resetting sensor signals, or sending reference signals to the controller. The host usually also allows to connect external hardware, which serves as an entry point for external signals, for example commanded by a pilot stick. This is represented by the Pilot Control block in Fig. 2. Together with a visualization such as a primary flight display (indicated in Fig. 1), this allows to even further increase possibilities with such a simulation-enhanced wind tunnel experiment.

3 Application Case: Integrated Roll and Gust Load Control

Building on the simulation-enhanced wind tunnel concept, this section details the application of the approach for validating an integrated primary flight and gust load alleviation controller. The controller simultaneously tracks roll commands and mitigates the effect of gust disturbances, which excite the flexible dynamics of the aircraft and thereby induce loads. Roll control follows an A320-style rate-command attitude-hold (RCAH) architecture [29], in which the controller tracks the roll rate commanded by the pilot with the side-stick, and maintains a constant roll angle when the stick is released. The gust load alleviation function targets the loads induced at the wing-root, the junction between wing and fuselage, as these are one of the drivers of structural weight [2].

Figure 3 illustrates a suitable sensor and control surfaces layout of a full aircraft configuration. The PFC function tracks the roll rate reference using direct measurements of p_b. In contrast, wing-root loads are not directly measurable in flight. Therefore, distributed wing acceleration measurements $\boldsymbol{y}_{\text{acc}}$ are used for GLA. The resulting objectives for the integrated control law are:

1. Primary Flight Control: Roll RCAH through reference tracking of the roll rate p_b, and disturbance rejection in the low frequency regime,
2. Aeroelastic Control: Attenuation of gust-induced wing-root bending moment $M_{\text{WR,x}}$ and torsion moment $M_{\text{WR,y}}$ (not depicted in the figure) using acceleration sensor feedback $\boldsymbol{y}_{\text{acc}}$,
3. Control activity and allocation: Efficient use of available ailerons $\boldsymbol{u}_{\text{ail}}$ with minimal control energy,
4. Stability and robustness: Nominal and robust stability under uncertainty, robust performance.

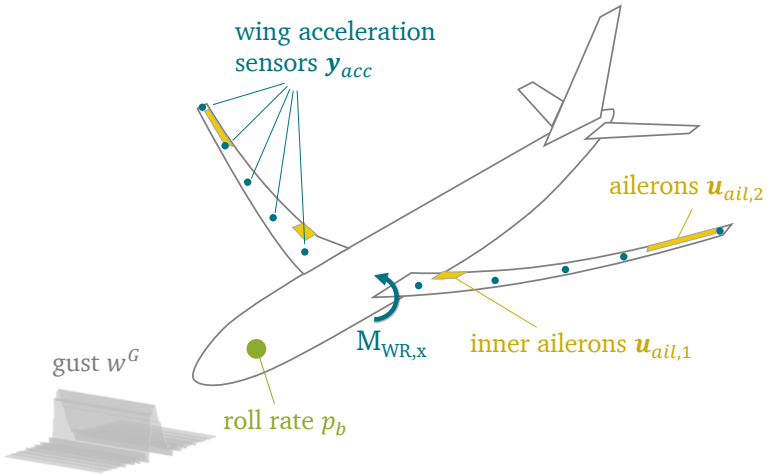

Fig. 3 Feedback sensors and control surfaces on the full aircraft representation.

The simulation-enhanced wind tunnel environment introduced in Section 2 allows to conceptually validate control laws developed for the full aircraft representation. Here, the setup consists of an aeroelastic wing in the wind tunnel, interconnected with a flight dynamics simulation and the real-time control law implementation. The wind tunnel setup is illustrated in Figures 4 and 5. The flexible model represents a long-range aircraft wing [24], featuring four trailing edge flaps and ten acceleration sensors, of which four are used in this work. The wing is mounted on a balance collecting force and moment data. A turn table allows to adapt the angle of attack. A gust generator [21] is installed upstream of the wing model, allowing to inject disturbances into the airflow.

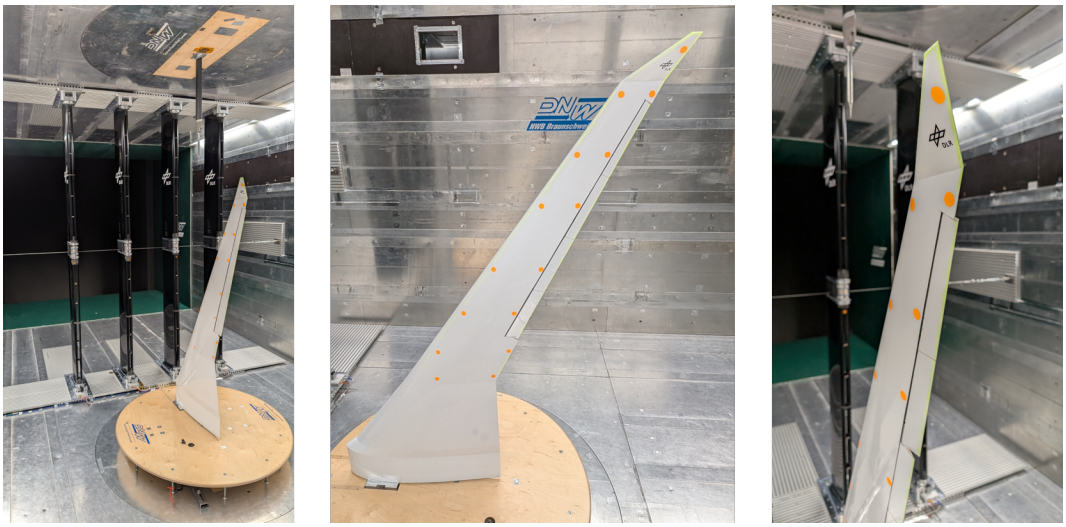

Fig. 4 Experimental setup of the wind tunnel test for integrated roll and gust load control.

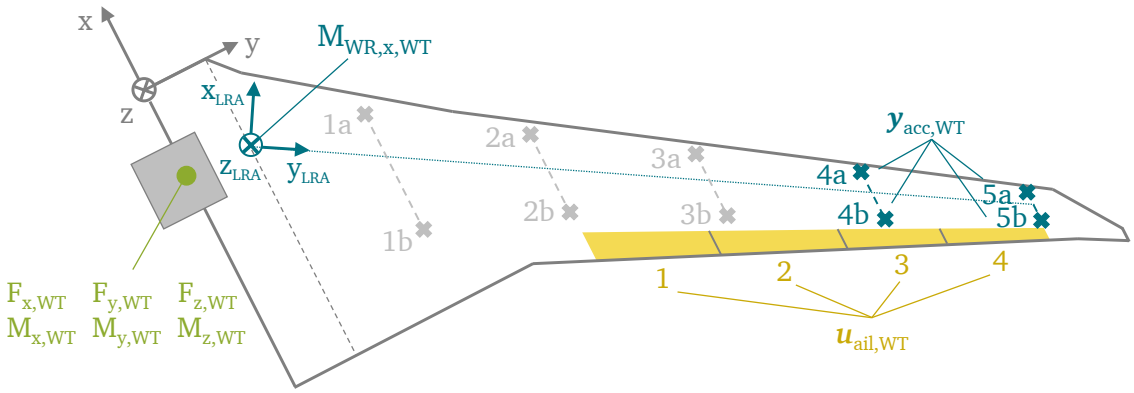

Fig. 5 Feedback sensors and control surfaces on the wind tunnel model.

A comparison between the component-level wing model in Fig. 5 and the free-flying aircraft in Fig. 3 highlights the differences that the simulation-enhanced wind tunnel setup shall resolve. Because the wing is physically clamped, it cannot execute an actual roll motion. To compensate, the aircraft simulation emulates the aircraft's roll dynamics about its longitudinal axis. Since the roll rate p_b cannot be measured directly, it is obtained within the simulation using the forces and moments measured by the balance. This will be explained in further detail below. While the framework is capable to augment the wind tunnel test with an aircraft simulation with full six degree-of-freedom longitudinal and lateral flight dynamics, the scope of the present work is limited to the roll axis to reduce complexity. Other characteristics remain consistent with the free-flying aircraft: wing-root bending and torsion moments remain non-measurable, instead, flexible dynamics are captured through acceleration sensors. The control surface configuration utilizes four outer-wing flaps, acting as both inboard and outboard ailerons.

Adapting the generic signal flow diagram presented in Fig. 2, the signal flow diagram for the present experiment is shown in Fig. 6, with its three main components of wind tunnel domain (experimental setup from Fig. 4), aircraft simulation domain (roll dynamics simulation), and real-time control law implementation. The signals to and from the wind tunnel block correspond to those indicated in Fig. 5. The simulation interface connects the sensor signals obtained in the data acquisition system to the aircraft

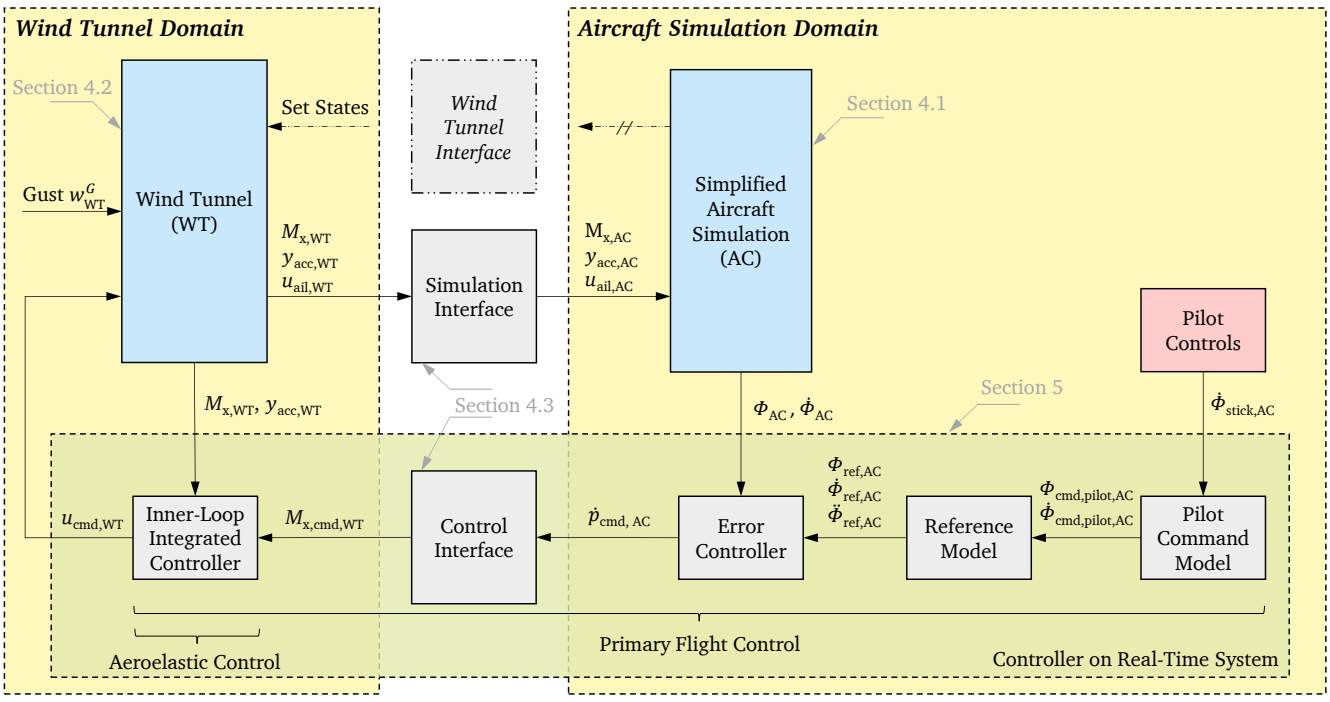

Fig. 6 Controller and signal flow diagram for the application case.

simulation. Scaling between the two different domains is indicated by the subscripts: *WT* denotes all signals in the wind tunnel domain, i.e. directly linked to the hardware and thus the model size; *AC* denotes all signals in the aircraft simulation domain, scaled and adapted for the full aircraft. Note that the wind tunnel interface is not connecting simulation and wind tunnel domain. In the present wind tunnel experiment it was not possible to pass data to the model motion block or wind tunnel condition block (compare with Fig. 2). Instead, operating conditions, angle of attack, and thus the states were set manually, indicated by *Set States* in the signal flow diagram.

The primary flight and aeroelastic controller deployed on the real-time system is operating in both wind tunnel and aircraft simulation domain, as discussed before. The architecture and individual components of the controller will be discussed in Section 5, detailing how to achieve the control objectives defined above. Before doing so, Section 4 will discuss the modeling of the aeroelastic aircraft and wind tunnel model, as well as the definition of the interfaces, to clarify the ingredients of the signal flow diagram, and allow for understanding of the designed controller. Figure 6 indicates the sections in which the respective components are discussed.

4 Aeroelastic Aircraft Modeling

A model of the aeroelastic aircraft is needed firstly to operate the simulation-enhanced wind tunnel test, i.e. provide the aircraft simulation, and secondly to provide the input for model-based controller design. To model the aeroelastic aircraft, the equations of motion for the rigid-body dynamics can be written based on the mean-axis formulation, assuming a flat, non-rotating earth, uniform gravity, constant mass and inertia tensor [30–32]:

$$\begin{bmatrix} m_b \cdot (\dot{\mathbf{V}}_b + \boldsymbol{\Omega}_b \times \mathbf{V}_b - \mathbf{T}_{bE} \cdot \mathbf{g}_E) \\ \mathbf{J}_b \cdot \dot{\boldsymbol{\Omega}}_b + \boldsymbol{\Omega}_b \times (\mathbf{J}_b \cdot \boldsymbol{\Omega}_b) \end{bmatrix} = \mathbf{P}_b^{\text{ext}}, \qquad \begin{aligned} \mathbf{V}_b &= [u_b, v_b, w_b]^T, \\ \boldsymbol{\Omega}_b &= [p_b, q_b, r_b]^T. \end{aligned} \tag{1}$$

The quantities in this equation are defined with respect to the body frame, at the aircraft's center of gravity (index b). The upper equation defines the translational dynamics, based on the velocity vector $\mathbf{V}_b$. The lower equation defines the rotational dynamics, using the rotational velocity vector $\boldsymbol{\Omega}_b$. Aircraft mass is denoted m_b, the inertia tensor $\mathbf{J}_b$, and the gravity vector $\mathbf{g}_E$ in the earth-centered-earth-fixed frame. Denoted on the right hand side are the external forces and moments $\mathbf{P}_b^{\text{ext}}$, which originate in aerodynamics, propulsion, and inertia forces of the flexible aircraft. The dynamics equation are complemented by the kinematics equations, that can be formulated as follows [29, 33]:

$$\begin{aligned} \dot{\mathbf{X}}_E &= \mathbf{T}_{bE}^T \cdot \mathbf{V}_b, & \mathbf{X}_E &= [x_E, y_E, z_E]^T, \\ \dot{\boldsymbol{\Phi}}_b &= \mathbf{M}_{bb} \cdot \boldsymbol{\Omega}_b, & \boldsymbol{\Phi}_b &= [\Phi_b, \Theta_b, \Psi_b]^T, \end{aligned} \tag{2}$$

where the translational kinematics map the velocity vector $\mathbf{V}_b$ to the position vector $\mathbf{X}_E$ in the earth-centered-earth-fixed system using the transformation matrix $\mathbf{T}_{bE}$, and the rotational kinematics map the rotational rates $\boldsymbol{\Omega}_b$ to the angular velocity $\dot{\boldsymbol{\Phi}}_b$, using the matrix $\mathbf{M}_{bb}$ that itself depends on the angles of pitch, roll, and yaw. To complete the description of the aeroelastic aircraft, the flexible dynamics need to be added. For linear structural dynamics these can be written in a modal formulation (index f) as [31, 32]:

$$\mathbf{M}_{ff} \cdot \ddot{\mathbf{u}}_f + \mathbf{B}_{ff} \cdot \dot{\mathbf{u}}_f + \mathbf{K}_{ff} \cdot \mathbf{u}_f = \boldsymbol{\Phi}_{gf}^T \cdot \mathbf{P}_g^{\text{ext}}, \tag{3}$$

where $\mathbf{u}_f$ is the modal deformation vector, and the matrices $\mathbf{M}_{ff}$, $\mathbf{B}_{ff}$, $\mathbf{K}_{ff}$ describe modal mass, damping, and stiffness, respectively. The right hand side reads the external forces and moments, this time denoted in the structural domain (index g). These are transferred into the modal domain using the eigenvector matrix $\boldsymbol{\Phi}_{gf}$. Note that rigid-body and flexible equations of motion are coupled through these external

loads [30]. This coupling is highlighted by expressing the body-frame loads from Eq. 1 as the projection of structural domain loads onto the (geometry-defined) rigid-body eigenvectors: $\mathbf{P}_b^{\text{ext}} = \mathbf{\Phi}_{gf}^T \cdot \mathbf{P}_g^{\text{ext}}$.

Equations 1 through 3 define the baseline of a nonlinear aeroelastic aircraft simulation. Further details on the underlying modeling components, particularly the external forces and moments, are provided in [32, 34]. The model is generated using the DLR-internal tool VarLoads [35, 36]. Augmented with sensors and actuators, the model can be used both for the aircraft simulation enhancing the wind tunnel experiment, see Section 4.1, and for model-based controller design, see Section 4.2.

4.1 Simplified Aircraft Simulation

In the setup presented in Section 3, the aircraft model is simplified to focus solely on roll dynamics about the longitudinal axis. Isolating this motion from Eq. 1, the roll acceleration $\dot{p}_b$ is defined as:

$$\dot{p}_b = \dot{\mathbf{\Omega}}_{b,y} = [\mathbf{J}_b^{-1} \cdot (\mathbf{M}_b^{\text{ext}} - \mathbf{\Omega}_b \times (\mathbf{J}_b \cdot \mathbf{\Omega}_b))]_y, \tag{4}$$

where the external moments $\mathbf{M}_b^{\text{ext}}$ are extracted as part of the loads vector $\mathbf{P}_b^{\text{ext}}$. This reduces even further when a linearization is performed, assuming that the rates and accelerations in pitch and yaw are small, and the inertia tensor partially zero, see [29]:

$$\dot{p}_b \approx \frac{1}{J_{xx}J_{zz} - J_{zx}^2} \cdot (J_{zz} \cdot M_{b,x}^{\text{ext}} + J_{zx} \cdot M_{b,z}^{\text{ext}}). \tag{5}$$

Although this constitutes a simplification of the aircraft's dynamics, it will not greatly effect the desired roll control test, and was chosen in this wind tunnel campaign for simplicity of implementation. Under the assumption of linearity (small angles), the rotational kinematics from Eq. 2 simplify to an identity between pitch rate and roll velocity, yielding the following relations:

$$\Phi_b = \int \dot{\Phi}_b, \quad \dot{\Phi}_b = p_b, \quad \ddot{\Phi}_b = \dot{p}_b. \tag{6}$$

Equation 5 and 6 form the simplified aeroelastic aircraft simulation model that is run in parallel to the wind tunnel experiment. Equation 5 requires the external moments $M_{b,x}^{\text{ext}}$ and $M_{b,z}^{\text{ext}}$ as an input. In the signal flow diagram in Fig. 6, it can be seen that the roll moment $M_{b,x,\text{WT}}^{\text{aero}}$ (of the wing component only, and only aerodynamic contributions) is obtained from the wind tunnel, scaled to aircraft level by the simulation interface. Note that the index b is omitted in the signal flow diagram for improved readability. The aerodynamic contributions of the other components (fuselage, empennage) are estimated based on the aircraft model. Additionally, the roll damping is estimated based on the predicted movement of the wing, and included in the moment term. Propulsive moments are disregarded in the setup. The yaw moment $M_{b,z}^{\text{ext}}$ is considered negligible as well.

With the mentioned simplification and constraints, Eqs. 5 and 6 define a simplistic roll dynamics simulation to be integrated in the aircraft simulation domain in Fig. 6, derived from the rigid-body dynamics of Eqs. 1 and 2. Flexible dynamics from Eq. 3 are not being simulated, as the dominant contributions arise from the wing physically present in the wind tunnel. Flexible effects from the fuselage and empennage are neglected. Although a more complete aircraft simulation (incorporating full rigid-body and flexible dynamics) could be implemented, this setup is sufficient to validate the roll RCAH and GLA control law and demonstrate the efficacy of the simulation-enhanced wind tunnel experiment.

4.2 Wind Tunnel Model

A model of the aeroelastic wing in the wind tunnel is not needed during the test, as it is physically present in the closed-loop system (wind tunnel domain in Fig. 6). However, it will be needed for model-based controller design, as described in Section 5. Since the wing is clamped at its root, this model

only considers the flexible dynamics of Eq. 3. A discussion on representing rigid-body dynamics within this clamped configuration follows in Section 4.3. The terms in Eq. 3 are generated using the DLR VarLoads environment [35, 36]. The structural properties including modal mass, damping, stiffness, and eigenvector matrices are derived from a finite element model, while aerodynamic loads are computed using the Doublet Lattice Method (DLM) [32]. The aerodynamics also cover a gust disturbance w^G induced upon the wing. This aeroelastic core is augmented with first-order actuator and sensor dynamics, and time delay. For an in-depth description of this modeling approach, see [34]. The result is a model in state-space representation, mapping the inputs of commanded control surface deflection and gust disturbance to the outputs of loads measured by the wind tunnel balance and acceleration measurements by the sensors near the wing tip:

$$\boldsymbol{G}_{WT}: \quad \left[\begin{array}{c} \dot{\boldsymbol{x}} \\ \hdashline \boldsymbol{y} \\ \boldsymbol{p} \end{array}\right] = \left[\begin{array}{c|cc} \boldsymbol{A} & \boldsymbol{B}_u & \boldsymbol{B}_d \\ \hdashline \boldsymbol{C}_y & \boldsymbol{D}_{yu} & \boldsymbol{D}_{yd} \\ \boldsymbol{C}_p & \boldsymbol{D}_{pu} & \boldsymbol{D}_{pd} \end{array}\right] \cdot \left[\begin{array}{c} \boldsymbol{x} \\ \hdashline \boldsymbol{u} \\ \boldsymbol{d} \end{array}\right] \qquad \begin{array}{ll} \boldsymbol{u} = \boldsymbol{u}_{\mathrm{cmd,WT}}, & \boldsymbol{d} = w^{\mathrm{G}}_{\mathrm{WT}}, \\ \boldsymbol{y} = \begin{bmatrix} M_{\mathrm{x,WT}} \\ \boldsymbol{y}_{\mathrm{acc,WT}} \end{bmatrix}, & \boldsymbol{p} = \begin{bmatrix} M_{\mathrm{WR,x,WT}} \\ M_{\mathrm{WR,y,WT}} \end{bmatrix}. \end{array} \tag{7}$$

The state-space model is in accordance with the inputs and outputs depicted in Fig. 6. Therefore, the load from the wind tunnel balance is only the roll moment, other forces and moments could be supplied if needed. Equation 7 sees the definition of an additional performance output $\boldsymbol{p}$, namely wing-root bending and torsion moment, at the origin of the loads reference axis (LRA), see Fig. 5. These quantities are non-measurable on the physical wind tunnel model, but are included in the numerical model for controller design, to allow targeting gust load alleviation.

4.3 Interfaces between Wind Tunnel and Simulation

Figure 6 illustrates the signal flow, where the simulation and control interface link the wind tunnel and aircraft simulation domain, while the wind tunnel interface is not available in this application case. The simulation interface transforms wind tunnel measurements for use in the simulation domain. The roll moment (and more generally the loads) measured by the wind tunnel balance are scaled to reflect full-scale aircraft values; wing-tip accelerations are transformed likewise. The measured control surface deflections are mapped directly to the aircraft without scaling.

An important consideration for clamped wing configurations is the lack of rigid-body motion. Unlike a free-flying aircraft, which alleviates additional aerodynamic loads such as gusts through natural flight path adjustments, a clamped model remains fixed. This results in significantly higher measured loads [27]. A model motion system can partially replicate these effects, as demonstrated in [27]. By imposing heave and pitch dynamics at the wing root, the rigid-body dynamics of Eqs. 1 and 2 can be mimicked. The respective motion would then be defined by the wind tunnel interface. However, the current setup lacks this capability. To compensate, the simulation interface could theoretically incorporate an artificial alleviation factor to reduce the gust-induced loads. As this would also reduce the measured roll moment, this option is not implemented here. Instead, lower-magnitude gusts are utilized to reduce the aerodynamic loads, while allowing for a representative evaluation of the control laws.

The control interface links the control law on aircraft level to the one on wind tunnel level. Beyond scaling between these domains, its purpose is signal emulation, which is necessary for the roll control law to be tested. As shown in Fig. 6 and further detailed in Section 5, the aircraft level controller outputs a commanded roll acceleration $\dot{p}_{b,\mathrm{cmd}}$. This is the typical command passed to a control allocation block to achieve the desired aircraft motion. Since roll acceleration cannot physically occur in a clamped wing configuration, the signal emulation within the control interface transforms commanded roll acceleration $\dot{p}_b$ to commanded roll moment $M_{b,x}$, based on the relationship established in Eq. 5. Combined with the scaling between aircraft and wind tunnel domain, the control interface reads:

$$M_{\mathrm{x,WT}} \approx \frac{1}{2} \cdot J_{\mathrm{xx,WT}} \cdot k_{\mathrm{WT\text{-}AC}} \cdot \dot{p}_{\mathrm{AC}}, \tag{8}$$

where the factor one half accounts for the single-wing setup in the wind tunnel (assuming symmetric contributions of both wings), and $k_{\mathrm{WT\text{-}AC}}$ represents the scaling between the domains. This relationship defines the representative experimental task: a simultaneous roll moment command and gust load alleviation, providing the foundation for the control design described in the following section.

5 Control Law Design

The integrated primary flight and aeroelastic control law is designed to fulfill the objectives established in Section 3. Its architecture is illustrated in Fig. 7, which is a mirrored version of the lower portion of the signal flow diagram from Fig. 6. The controller employs a cascaded structure consisting of an outer-loop rate-command attitude-hold (RCAH) system, and an integrated inner-loop. The outer-loop tracks commanded roll rates (roll angular velocities) and maintains attitude when the rate command returns to zero, following a standard PFC architecture, as used for instance in nonlinear dynamic inversion (NDI) control implementations [37, 38].

The inner-loop introduces a novel feature compared to traditional implementations. While standard primary flight control typically employs an open-loop control allocation to execute roll acceleration commands, the approach presented here establishes a closed-loop on this innermost variable. The system tracks the roll acceleration, which is emulated via the measured roll moment as described in Section 4.3. Furthermore, the inner-loop incorporates the aeroelastic control functionality for gust load alleviation, resulting in an integrated inner-loop control law, as proposed in [28]. The following sections provide a functional overview of the controller components, moving from the outer to the inner loop.

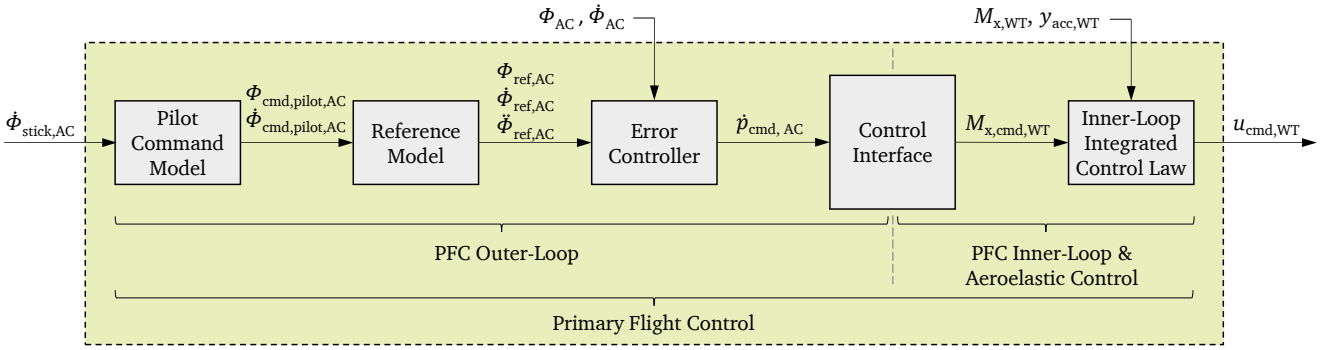

Fig. 7 Architecture of the integrated primary flight and aeroelastic control law.

5.1 Outer-Loop Control Law

The outer-loop primary flight control architecture comprises a pilot command model, a reference model, and an error controller to realize the RCAH functionality. This outer-loop transforms pilot stick inputs (roll velocity commands) into a commanded roll acceleration, which is then passed to the inner-loop control law. While the architecture follows those of NDI designs [37], other implementations for the outer-loop remain feasible. The specific design presented here is developed in [39] for evaluating (incremental) nonlinear dynamic inversion flight control functions, and inspired by the A320 flight control system [29]. Figure 8 shows the first two components: pilot command and reference model.

The pilot command model processes roll rate (roll angular velocity) stick inputs $\dot{\Phi}_{\mathrm{stick}}$ to generate pilot-commanded roll angle $\Phi_{\mathrm{cmd,pilot,AC}}$ and roll rate $\dot{\Phi}_{\mathrm{cmd,pilot}}$, while imposing the RCAH logic and several envelope protections. Specifically, the pilot command model implements a blending between

rate-command attitude-hold and direct attitude control functionality [39]. Within the standard roll angle range, here ± 35°, the RCAH mode is active: the stick-commanded roll rate passes through the upper signal path, while the pilot-commanded roll angle is derived by integrate that same rate. An upper limit on the roll rate is implemented, here to a value of ± 15°/s. In this mode, releasing the stick maintains the current roll angle. When the roll angle exceeds the threshold of ± 35°, up to a hard limit of ± 60°, the system transitions to attitude control. In this regime, the stick input is routed to the lower signal path to directly command the roll angle, while the rate path is set to zero. To allow a smooth transition between these modes, the attitude control gain is defined by a relative damping ζ and natural frequency ω_0 consistent with the reference model.

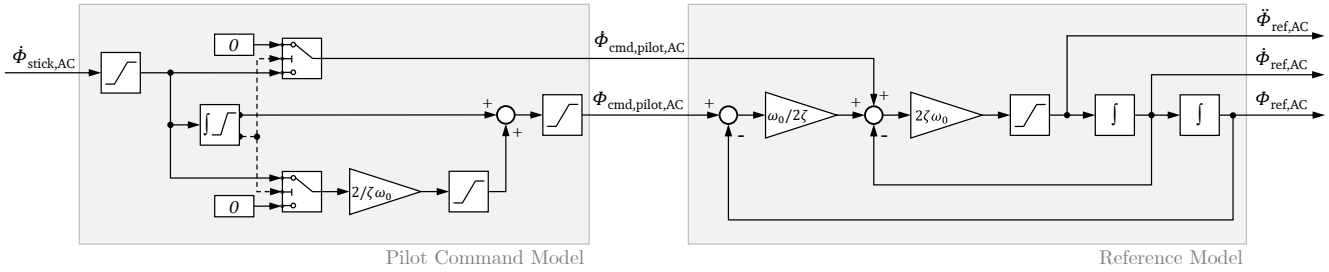

Fig. 8 Pilot command and reference model of the developed control law.

Pilot-commanded roll angle and rate command are passed into the reference model. This second-order model transfers the commands into an ideal reference in angle Φ_{ref}, rate $\dot{\Phi}_{\text{ref}}$, and acceleration $\ddot{\Phi}_{\text{ref}}$, that the error and inner-loop controller shall track. The otherwise standard implementation is augmented with the rate feedforward from the pilot command model, in order to reduce phase lag and expedite the buildup of the reference. The reference model includes gains with tunable parameters, to set the desired reference dynamics: the natural frequency ω_0, determining the speed of the tracking, and the relative damping ζ, trading rise time of the response with an overshoot above the desired reference. These two parameters are also included in the pilot command model, as discussed above. They are selected or tuned based on the aircraft of application. In the presented experiment, a relatively slow dynamic of $\omega_0 = 2$ rad/s was set, while the damping was set at $\zeta = 0.8$.

The reference roll acceleration is fed forward directly to the commanded roll acceleration $\dot{p}_{\text{cmd,AC}}$, while the reference roll angle and rate are processed by the error controller shown in Fig. 9. This controller ensures tracking of angle and rate using a PID-based design receiving feedback signals from the aircraft. Proportional, integral, and derivative paths are all routed through a common integrator, to allow for easy implementation of anti-windup strategies (not part of this paper). The parameters of the controller can either be tuned manually, or using a multi-objective parameter synthesis such as developed in [40]. This component concludes the outer-loop controller design, that is deployed on aircraft level.

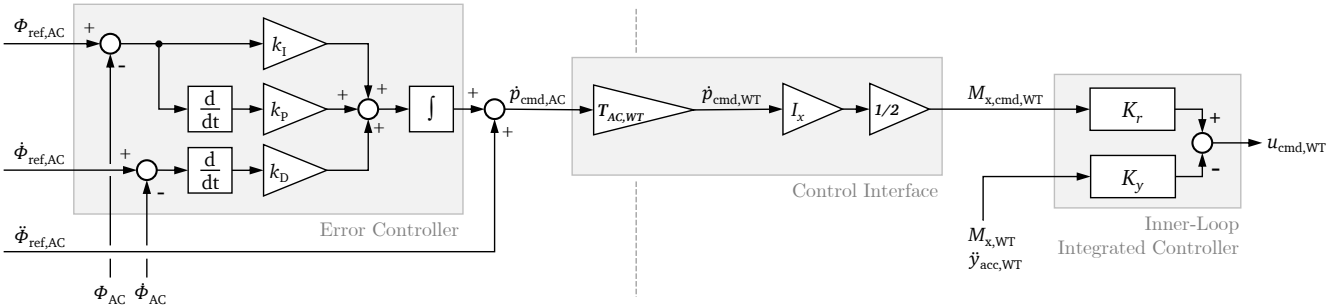

Fig. 9 Error controller, control interface, and inner-loop of the developed control law.

In a standard PFC architecture, such as NDI, the commanded roll acceleration $\dot{p}_{\text{cmd,AC}}$ is mapped to the control surfaces using a control allocation scheme. In the strategy proposed here, however, this

acceleration is actively controlled. This necessitates feedback of the roll acceleration, which can be provided by angular accelerometers on free-flying aircraft. Although not common for state-of-the-art passenger aircraft, these sensors are available and have proven to be beneficial for implementation of so-called incremental control methods [41]. In the current wind tunnel setup, the roll acceleration is non-measurable, therefore emulated by the feedback of the roll moment, as outlined in Section 4.3. The control interface bridges between outer-loop and inner-loop control.

5.2 Inner-Loop Integrated Control Law

The inner-loop controller combines roll acceleration (roll moment) tracking with gust load alleviation, forming the core of the integrated primary flight and aeroelastic control law. For an aeroelastic aircraft, tracking roll acceleration in addition to roll rate is beneficial, as the rigid-body dynamics are influenced by the flexible dynamics. This inherent coupling between rigid-body and flexible dynamics is also the rational of performing an integrated control design, rather than a separated approach for designing primary flight and aeroelastic control. Additionally, since both control functions are realized using the same set of control surfaces, an integrated controller provides an effective framework for managing the necessary trade-off to fulfill all control objectives.

The inner-loop controller is developed using μ-synthesis robust control [42–44]. This is an effective method for this application case, because it allows numerous (often conflicting) control objectives to be formulated within a joint optimization setup using weighting functions, without imposing a certain controller structure. In aeroelastic control, the optimal pairing of actuators and sensors is less obvious than in PFC, therefore, an unstructured synthesis that optimizes these multi-variable interactions is beneficial. The weighting functions encode the control objectives, including tracking performance, disturbance rejection, and control allocation. Additionally, robustness is a key requirement to ensure reliable controller performance even under uncertainty. This is explicitly addressed by μ-synthesis, which incorporates uncertainty directly into the plant model [45].

The synthesis setup in closed-loop configuration is shown in Fig. 10, illustrating the control architecture and the interconnection with the aeroservoelastic design model defined in Eq. 7. The plant model $\boldsymbol{G}$ represents the wind tunnel wing $\boldsymbol{G}_{\mathrm{WT}}$, where the subscript is omitted here for clarity. In the figure, the plant model sees the same inputs and outputs as in Eq. 7, namely control commands $\boldsymbol{u}_{\mathrm{cmd}}$, gust disturbance w^G, feedback variables M_x and $\boldsymbol{y}_{\mathrm{acc}}$, and performance outputs $M_{\mathrm{WR,x/y}}$. The plant is augmented with uncertainty, indicated by the tilde and discussed below. The controller combines feedforward action $\boldsymbol{K}_r$ and feedback $\boldsymbol{K}_y$ action to track the reference command $\boldsymbol{r}$, here the roll moment $M_{x,\mathrm{cmd}}$, and suppress the gusts disturbances. To impose tracking requirements, the tracking error is formulated between the feedback signal and the ideal reference $\boldsymbol{r}_{id}$ generated by the filter $\boldsymbol{W}_{ref}$. The loop is closed by connecting the feedback signals to the controller, which are subject to noise $\boldsymbol{n}$.

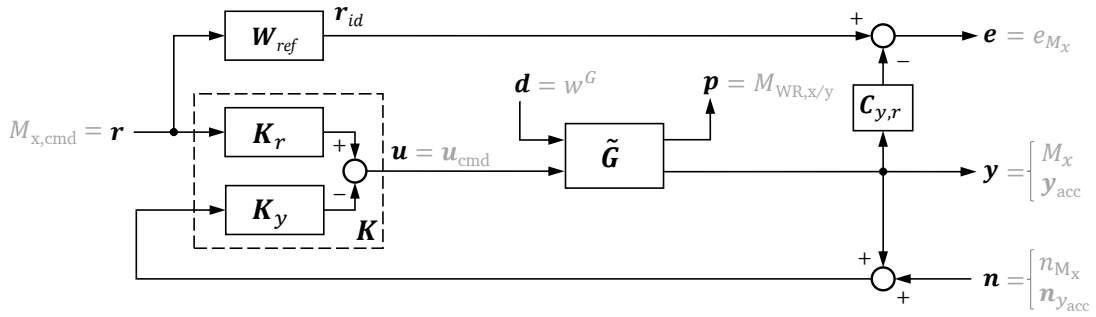

Fig. 10 Synthesis setup for the inner-loop integrated controller.

The ideal reference is generated by passing the reference signal through the filter $\boldsymbol{W}_{ref}$. The architecture presented here constitutes implicit model-following, where the reference dynamics are not explicitly

embedded within the controller, but implicitly adhered to during the synthesis. The tracking filter is designed as a second order filter, with a roll-off frequency between 5 and 10 rad/s. The selection of this tracking frequency poses a trade-off between tracking and load alleviation capabilities: the faster the demanded tracking, the lower the available bandwidth for load alleviation, due to the link between performance and robustness and hence inherent constraints on shaping the sensitivity functions (waterbed effect) [46]. The selection of this filter must be coordinated with the parameters set in the reference model, as described in Section 5.1.

In robust control, specific closed-loop transfer functions connecting exogenous inputs and outputs are selected and weighted for inclusion in the H_∞-norm, which the synthesis algorithm seeks to minimize. This approach enables the systematic shaping of these transfer functions to achieve the desired dynamic behavior of the closed-loop system [42]. The transfer functions selected for the integrated controller are summarized in Table 1. The following abbreviations for the sensitivity functions are used, derived based on the partitioned plant of Eq. 7: input sensitivity $\boldsymbol{S}_i = (\boldsymbol{I} + \boldsymbol{K}_y\boldsymbol{G}_{yu})^{-1}$, output sensitivity $\boldsymbol{S}_o = (\boldsymbol{I} + \boldsymbol{G}_{yu}\boldsymbol{K}_y)^{-1}$, input complementary sensitivity $\boldsymbol{T}_i = \boldsymbol{K}_y\boldsymbol{G}_{yu} \cdot \boldsymbol{S}_i$, and output complementary sensitivity $\boldsymbol{T}_o = \boldsymbol{G}_{yu}\boldsymbol{K}_y \cdot \boldsymbol{S}_o$. The error $\boldsymbol{e}$ on the roll moment is weighted such that tracking is achieved in the low frequency regime, as well as disturbance rejection. All feedback variables (roll moment, acceleration sensors) $\boldsymbol{y}$ are weighted to ensure robust stability, and to shape sensor usage in the respective frequency ranges. The control commands $\boldsymbol{u}$ are weighted to shape the applied control energy, to roll-off in the high frequency range, and to attenuate noise in said range. Finally, the performance output $\boldsymbol{p}$ of the wing-root moments is used to achieve the desired gust load alleviation, focused on the first flexible eigenmode.

Table 1 Relevant closed-loop transfer functions and weights to shape these.

Objective	**Sensitivity to shape**		
	Name	**Formula**	**Channel**
Reference Tracking	Feedforward Sensitivity	$\boldsymbol{W}_{ref} - \boldsymbol{S}_o\boldsymbol{G}_{yu}\boldsymbol{K}_r$	$\boldsymbol{r} \rightarrow \boldsymbol{e}$
Disturbance Rejection	Disturbance Sensitivity	$\boldsymbol{S}_o\boldsymbol{G}_{yd}$	$\boldsymbol{n} \rightarrow \boldsymbol{e}$
Aeroelastic Performance	Performance Load Sensitivity	$\boldsymbol{G}_{pd} - \boldsymbol{G}_{pu}\boldsymbol{K}_y\boldsymbol{S}_o\boldsymbol{G}_{yd}$	$\boldsymbol{d} \rightarrow \boldsymbol{p}$
Control Activity	Feedforward Control Sensitivity	$\boldsymbol{S}_i\boldsymbol{K}_r$	$\boldsymbol{r} \rightarrow \boldsymbol{u}$
	Feedback Control Sensitivity	$\boldsymbol{K}_y\mathbf{S}_o$	$\boldsymbol{n} \rightarrow \boldsymbol{u}$
Sensor Usage	Complementary Sensitivity	$\boldsymbol{T}_o$	$\boldsymbol{n} \rightarrow \boldsymbol{y}$
Nominal Stability			

To enforce robustness in the control design, uncertainties are incorporated into the plant model used for the synthesis. Multiplicative structured uncertainty [42] is implemented at both the plant input and the output, representing variations in actuators and sensors, respectively. These uncertainties are selected based on physical insight and are designed to increasing in magnitude at higher frequencies. The complex uncertainties impose both gain and phase deviations, thereby encoding unknown or unmodeled dynamics, model mismatches, and variations in operating conditions. The resulting uncertain plant is defined as:

$$\tilde{\boldsymbol{G}} = (\boldsymbol{I} + \boldsymbol{W}_o\boldsymbol{\Delta}_o) \cdot \boldsymbol{G} \cdot (\boldsymbol{I} + \boldsymbol{W}_i\boldsymbol{\Delta}_i), \qquad \boldsymbol{\Delta}_{i/o} = \mathrm{diag}(\delta_{i/o,m}),\ \|\boldsymbol{\Delta}_{i/o}\|_\infty < 1, \tag{9}$$

where $\boldsymbol{\Delta}_{i/o}$ encodes the diagonal matrix of structured uncertainty at the inputs or outputs, consisting of complex uncertainty elements δ_m. The diagonal weighting matrices $\boldsymbol{W}_i$ and $\boldsymbol{W}_o$ define the frequency dependent magnitude of these uncertainties and are chosen to reflect the worst-case system behavior.

A comprehensive description of the inner-loop integrated control design is provided in [28], including the selection of weighting functions to achieve the desired closed-loop shapes from Table 1, and detailed information on the uncertainty modeling. That work also contains further explanations on the synthesis mechanism, and the evaluation of the control law. The following section details the evaluation of the combined RCAH and GLA controller within the experimental framework.

6 Experimental Validation and Results

The integrated primary flight and aeroelastic controller is validated at the German-Dutch low-speed wind tunnel in Braunschweig (DNW-NWB), utilizing the simulation-enhanced wind tunnel test concept. The setup is illustrated in Section 3, see the signal flow diagram in Fig. 6. The tests are performed at a freestream velocity of 30 m/s, at atmospheric conditions, the wing model is set to 0° angle of attack. The controller described in the previous section is discretized and executed on a real-time system, with a sample frequency of 1000 Hz. The system also runs the simplified aircraft simulation model at the same frequency. The actuators are operated by PWM signals at 560 Hz, the data acquisition system provides information at 3000 Hz. Further information on the wind tunnel campaign is given in [47].

To validate the primary flight control function of roll rate-command attitude-hold, a roll rate stick command is given to the controller, as illustrated in Fig. 6. In the test setup, an actual joystick is used and connected to the host computer that controls the real-time system. The current roll attitude is visualized on a simulated primary flight display (artificial horizon), as schematically indicated in Fig. 1. This allowed to "fly" the aircraft in the simulation-enhanced wind tunnel setup. Alternatively, the roll rate commands are provided using a graphical user interface on the host computer.

The results of one validation scenario are displayed in Fig. 11. In this scenario, the stick is first deflected fully to the right, commanding a roll rate p_{stick} of 15°/s, as shown by the black line in Fig. 11b. This leads to a reference roll rate p_{ref} being generated by the reference model, displayed as the blue line in the same figure, smoothed out compared to the commanded roll rate. The actual roll rate p is able to track the reference roll rate quite closely, indicating good tracking properties and well-matched dynamics in the different controller loops. If the inner-loop integrated controller were too slow, the roll rate would not be able to track the reference roll rate. The good tracking capabilities can also be observed in Fig. 11c, in which reference roll moment, ideal reference roll moment, and actual roll moment are closely related. To achieve the desired roll rate the flaps are deflected upwards on the right wing, leading to decreased lift on this wing and inducing the roll motion to the right, see Fig. 11d. The maximum allowed roll rate is achieved relatively fast, then the roll acceleration, i.e. roll moment, and the flaps return towards zero.

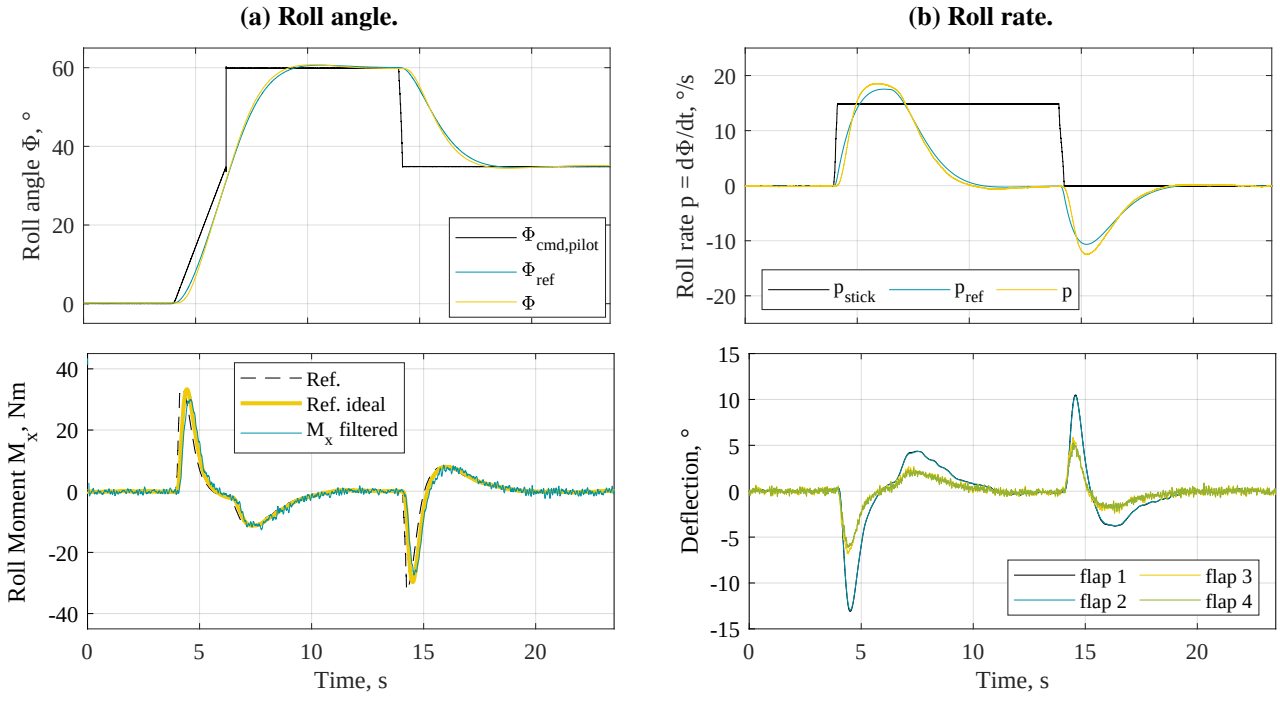

Fig. 11 Roll angle, rate, moment, and control commands during a full stick and release maneuver.

Note that the flaps deflect to different extents. The inner flaps 1 and 2 deflect by about twice as much as the outer flaps 3 and 4. This is an intentional design specified in the inner-loop integrated controller: all flaps shall contribute to the reference tracking task, while only the outer two flaps contribute to the gust load alleviation task. To reserve bandwidth for the load alleviation task, in case the gust acts simultaneously to the roll maneuver, the control allocation is performed in such a way that the outer flaps only use about half as much deflection for tracking the reference as the inner flaps. This was achieved by an individual shaping of the weighting function imposed on the control command, see [28] for details.

The deflection of the stick leads to the roll angle building up, as shown in Fig. 11a. The commanded roll angle $\Phi_{cmd,pilot}$ (black line) is computed based on the commanded roll rate, therefore increases by 15°/s. Tracking of the roll angle is also satisfactory, as the match between reference angle Φ_{ref} (blue line) and actual angle Φ (yellow line) shows. At about 6 seconds, the roll angle exceeds the value of 35°. As described in section 5.1, this alters the control function from a rate tracking to an angle tracking. With the stick still deflected fully to the right, the commanded roll angle now reads 60°, the maximum allowed. The roll rate is decreased as not to overshoot this value, leading to a negative roll acceleration and thus moment, as well as flap deflection. This slows down the speed of the roll motion. As soon as the maximum roll angle is reached, the roll rate, moment, and flap deflection remain at zero.

After the stick is released at about 14 seconds, the commanded roll angle drops back to 35°, the commanded roll rate is zero, yielding a roll angle reference that now slowly approaches the commanded value. To do so, a negative roll rate reference is generated, again closely tracked by the actual roll rate, see Fig. 11b. Roll moment and flaps now deflect into the opposite direction, generating a roll motion to return the attitude to a bank angle of 35°. As soon as this angle is reached, the rate, moment, and flap commands also reach zero.

In a second scenario, the stick is deflected in an alternating left-right movement, with occasional return to zero, trying not to exceed a roll angle of 35°, such that the controller remains in the rate command setting. The results are depicted in Fig. 12. Figure 12a and 12b reveal a close match between the reference roll angle and rate and the actual roll angle and rate (blue and yellow lines), while there is a certain difference to the signals commanded by the stick (black lines). This indicates that the

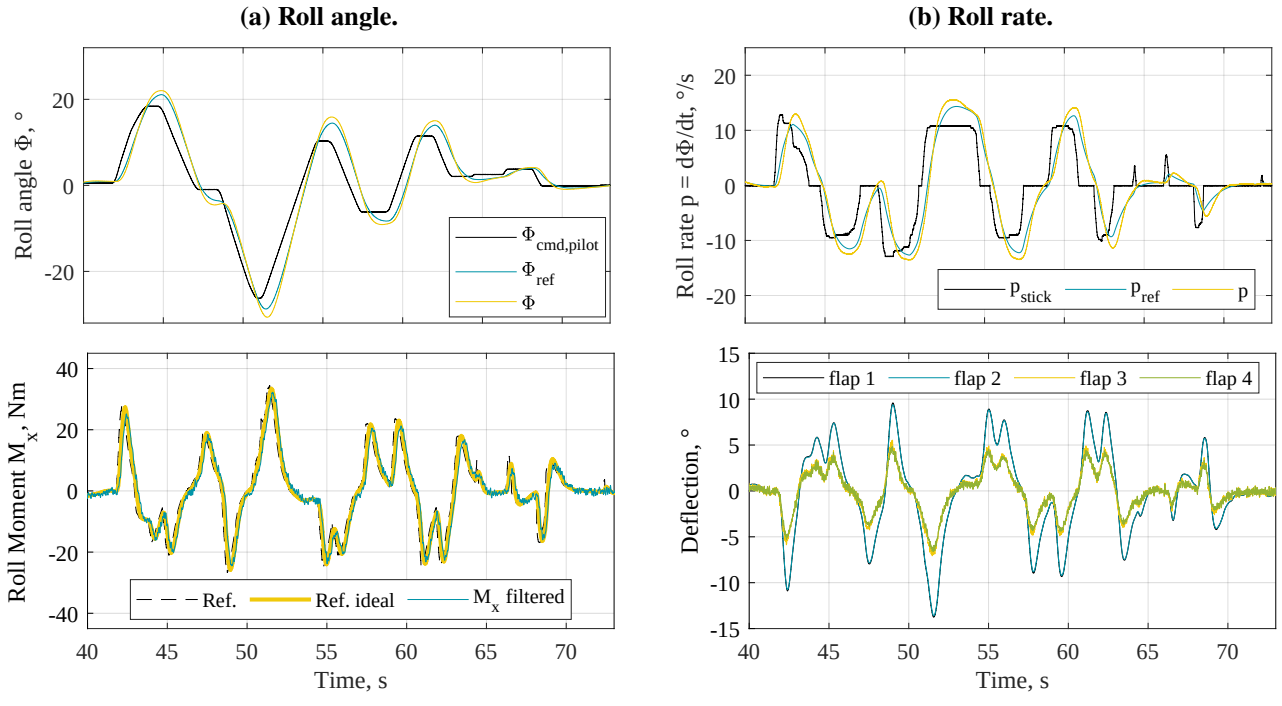

Fig. 12 Roll angle, rate, moment, and control commands during a left-right stick maneuver.

reference model introduces some delay, due to the chosen parameters for frequency ω_0 and damping ζ, see section 5.1. For a closer match of the signals a faster outer-loop dynamic is needed, which then necessitates an even faster inner loop. If the controller shall be improved in terms of tracking and handling qualities, this would need to be addressed.

The commands send to the inner-loop are tracked with satisfactory accuracy, as revealed by the roll moment (emulated pitch acceleration) displayed in Fig. 12c. Note that the commanded roll moment is essentially the derivative of the reference roll rate, yielding twice as many peaks as in the rate plot. The flap deflection commands presented in Fig. 12d are directly linked to the commanded roll moment. As in the first scenario, the outer flaps deflect only about half as much as the inner flaps, due to the specified control allocation. The maximum allowed flap deflection was defined to be ±15°. The inner flaps deflect close to this limit when the controller reaches the maximum allowed roll rate, but the limit is respected. The inner flaps have sufficient margin, they do not deflect more than 7°, preserving sufficient control authority for the secondary aeroelastic function, even when the maximum roll rate is commanded. When the rate command returns to zero, also the flaps return to their zero position.

Having validated the primary flight control function of roll tracking, the third scenario presented here is concerned with gust load alleviation. For this scenario, the reference (roll rate command) is kept at zero. The gust generator (see Fig. 4) then induces a continuous harmonic gust that excites the flexible wing. After some time the controller is turned on, to analyze the load alleviation capabilities. The result is depicted in Fig. 13, where roll moment is plotted over time. Note that this roll moment measured by the wind tunnel balance can be seen as an equivalent wing-root bending moment. The actual bending moment is defined with respect to the loads reference axis (LRA), as indicated in Fig. 5. The measured roll moment could be transferred to this wing-root bending moment, but this step is omitted within this paper, as both quantities resemble each other quite closely. Figure 13 shows the roll moment response of the wing to a gust with a frequency of 8.5 Hz, which is close to the first flexible eigenfrequency of the wind tunnel model (wing bending), and therefore yields the highest loads.

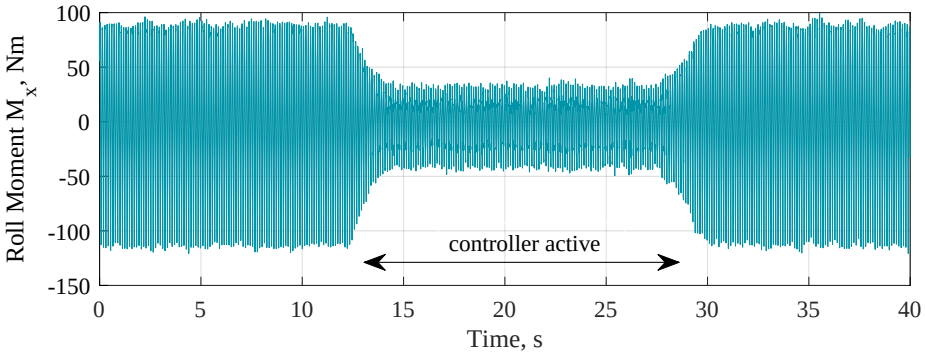

Fig. 13 Reduction in roll moment (≈ bending moment) with active integrated controller.

As observed in the figure, the bending moment can be substantially reduced when the controller is active. The relative reduction of the root-mean-square value reads 66% when referring to the Delta in roll moment induced by the gust. The anti-symmetry of the roll moment in positive and negative direction is linked to the gust generator, that induces a larger updraft (positive lift, negative roll moment) than downdraft. The reduction in bending moment is also presented in Fig. 14a, there as an overlay of time excerpts with and without active controller and hence gust load alleviation (GLA). The necessary flap deflection commands to achieve the load alleviation are plotted in Fig. 14b. Now the control allocation once again is visible: the inner flaps 1 and 2 are not used for load alleviation, but only for tracking purposes, while the outer flaps 3 and 4 are used for both, and now achieve the load reduction. The maximum commanded deflection does not exceed 8°, leaving sufficient control authority for a roll command that might be given simultaneously.

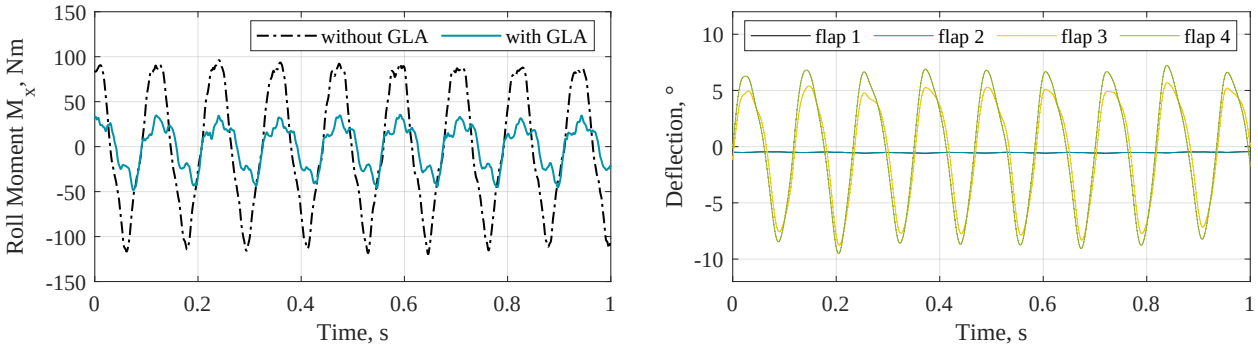

(a) Roll moment (≈ bending moment). **(b) Flap commands during active controller.**

Fig. 14 Roll moment and commanded flap deflections during a gust encounter.

With these scenarios, the integrated roll RCAH and GLA controller is successfully validated using the simulation-enhanced wind tunnel experiment. The setting allows to investigate the performance of the controller in various conditions and maneuvers, of which only three were shown as examples. By enhancing the wind tunnel experiment, not only the aeroelastic control function could be tested, but also the primary flight control, and the interplay and coordination between the functions.

7 Conclusions

This paper presents a strategy for simulation-enhanced wind tunnel testing, that allows the validation of primary flight and secondary control functions, with a focus on testing for aeroelastic aircraft. The idea is to replicate the aeroelastic properties of the aircraft under test as closely as possible on a wind tunnel model. To do so, and to account for the limitations of the wind tunnel, only a component of the aircraft (e.g. wing, empennage, or half-model) is placed inside the tunnel, while an aircraft simulation integrates the obtained measurements and provides the remaining quantities needed for controller testing. Interfaces between wind tunnel and simulation domain account for signal scaling and emulation, such that the relevant signals are available in either domain. A designed controller is then deployed in one, the other, or both domains, and is fed with the signals relevant for validation. The schematic signal flow diagram is presented, showing the integration of the different components, adaptable to a variety of tests.

The concept of simulation-enhanced wind tunnel testing is then demonstrated using the example of a roll rate-command attitude-hold controller combined with gust load alleviation. Having presented the experimental setup, the generic signal flow scheme is adapted to the test example, to further improve understanding of the proposed testing concept. The example shares details on the implemented model, controller design, and finally presents the results obtained in the wind tunnel test. Thereby, the effectiveness of the proposed simulation-enhanced wind tunnel experiment is demonstrated: it was possible to investigate the performance of the primary flight and aeroelastic controller, and how the functions interact. For example, the necessary adaptation of inner- and outer-loop dynamics based on the various filters and gains to be tuned was analyzed. Such an investigation would not have been possible by purely testing the wing model in the experiment, showcasing the merits of the proposed testing concept.

Future work is suggested in maturing the proposed concept: the example presented here uses a simplified aircraft simulation model, with isolated roll dynamics. While serving the purpose of conceptually demonstrating the idea, future work should aim at integrating a full nonlinear aircraft simulation within the enhanced wind tunnel test. With a full aircraft simulation also interactions of all rigid-body dynamics (and kinematics) with the flexible dynamics could be investigated. Furthermore interesting would be to conduct wind tunnel tests using an aeroelastic half-model of the aircraft including fuselage and tail, that allows to not only mimic roll dynamics, but also pitch dynamics. If the model

motion system were able to generate fast pitch and heave dynamics, the obtained aerodynamic behavior is even closer to that of a free-flying aircraft. With such a hardware setup, simulation-enhanced wind tunnel testing could strongly benefit flight control development for future aircraft concepts, under safe and reproducible conditions, early on in the design process.

Acknowledgments

The authors would like to thank all contributors involved in planning, preparation and execution of this wind tunnel experiment, making the controller test possible. Special thanks to Charlotte Hanke, Thomas G. Schmidt, Anna Altkukatz, Marc Braune, and Holger Mai (test execution, gust generator design, measurement technology and data acquisition), Johannes Dillinger (wind tunnel model development and finite element modeling), Robin Volkmar, Keith Soal, and Marc Böswald (structural identification of the model), Simon Schulz, and Ramesh Konatala (support system identification controller testing), Manuel Pusch (support during controller development), Spilios Theodoulis (support during controller development), and the wind tunnel team of the DNW-NWB.

Declaration of Use of Artificial Intelligence

Artificial intelligence was used in this work only to improve language and style of writing. Artificial intelligence was not used to generate scientific content, develop ideas, perform analysis, or produce results. All concepts, methods, data, and conclusions presented are entirely those of the authors.

References

[1] Markus Dino Krengel. *Load Alleviation and Wing Planform Optimization for Fuel Efficient Conceptual Aircraft Design*. PhD thesis, Technical University Braunschweig, Braunschweig, Germany, 2025. doi: 10.57676/0ae9-hz13.

[2] Simon Binder. *Simultaneous Optimisation of Composite Wing Structures and Control Systems for Active and Passive Load Alleviation*. PhD thesis, Delft University of Technology, Delft, Netherlands, 2021. doi: 10.4233/uuid:fac93ccf-7e0b-4971-a797-d2617e378a1d.

[3] Christopher D. Regan and Christine V. Jutte. Survey of Applications of Active Control Technology for Gust Alleviation and New Challenges for Lighter-Weight Aircraft. Technical Report, TM-2012-216008, NASA, 2012. `https://ntrs.nasa.gov/citations/20120013450`.

[4] H. Höhnlinger, H. Zimmermann, O. Sensburg, and J. Becker. Structural Aspects of Active Control Technology. In *Flight Mechanics Panel Symposium, AGARD Conference Procedings 560*, Turin, Italy, 1994. Advisory Group For Aerospace Research and Development of NATO (AGARD). `https://apps.dtic.mil/sti/tr/pdf/ADA292046.pdf`.

[5] Martin Hanel. Integrated Flight and Aeroelastic Control of a Flexible Transport Aircraft. In *AIAA Guidance, Navigation, and Control Conference and Exhibit*, number AIAA 98-4297, Boston, USA, 2019. AIAA. doi: 10.2514/6.1998-4297.

[6] Klaus König and Jörg Schuler. Integral Control of Large Flexible Aircraft. In *RTO Meeting Proceedings 36, Structural Aspects of Flexible Aircraft Control*, number ADA388195, Ottawa, Canada, 1994. Research and Technology Organization (RTO) of NATO. `https://apps.dtic.mil/sti/citations/ADA388195`.

[7] Mario Garcia-Sanz. Control Co-Design: An Engineering Game Changer. In *Advanced Control for Applications*, volume 1, 2019. doi: 10.1002/adc2.18.

[8] Reiko Mueller and Markus Ritter. Virtual Flight Testing of a Controller for Gust Load Alleviation using FMI for Cosimulation. In *Proceedings of the 12th International Modelica Conference*, Prague, Czech Republic, 2017. doi: 10.3384/ecp17132921.

[9] Philipp Heinrich, Patrick Meyer, Enno Brokof, Christoph Naue, and Christian Hühne. Electric Drive Systems for Multifunctional Trailing-Edge Control Surfaces: Dynamic and Thermal Characterization under Simulated Flight Loads. *Aerospace Science and Technology*, 168(C), 2026. doi: 10.1016/j.ast.2025.110824.

[10] Felix Stalla, Gertjan Looye, Thiemo M. Kier, Kolja Michel, Markus Ritter, Thomas G. Schmidt, Johannes Dillinger, and Martin Tang. Wind Tunnel Testing Active Gust Load Alleviation on an Experimental Wing. In *International Forum on Aeroelasticity and Structural Dynamics (IFASD) 2024*, Den Haag, Netherlands, 2024. `https://elib.dlr.de/205523/`.

[11] Martin R. Waszak. Robust Multivariable Flutter Suppression for Benchmark Active Control Technology Wind-Tunnel Model. *Journal of Guidance, Control, and Dynamics*, 24(1), 2001. doi: 10.2514/2.4694.

[12] Balint Vanek, Béla Takarics, Daniel Balogh, Tamás Luspay, Thiemo M. Kier, Keith Soal, Ramesh Konatala, Nicolas Guerin, and Julius Bartasevicius. Flight Testing Active Flutter Suppression Technologies, the European FliPASED Perspective. In *AIAA SciTech 2025 Forum*, Orlando, USA, 2025. doi: 10.2514/6.2025-1851.

[13] David K. Schmidt, Brian P. Danowsky, Aditya Kotikalpudi, Julian Theis, Christopher D. Regan, Peter J. Seiler, and Rakesh K. Kapania. Modeling, Design, and Flight Testing of Three Flutter Controllers for a Flying-Wing Drone. *Journal of Aircraft*, 57(4), 2020. doi: 10.2514/1.C035720.

[14] K.-U. Hahn and R. König. ATTAS Flight Test and Simulation Results of the Advanced Gust Management System LARS. In *AIAA Guidance, Navigation and Control Conference*, number 92-4343-CP, Hilton Head, USA, 1992. AIAA. doi: 10.2514/6.1992-4343.

[15] Kenneth L. Roger, Garold E. Hodges, and Larry Felt. Active Flutter Suppression - A Flight Test Demonstration. *Journal of Aircraft*, 12(6), 1975. doi: 10.2514/3.59833.

[16] Min Huang and Zhong-wei Wang. A Review of Wind Tunnel Based Virtual Flight Testing Techniques for Evaluation of Flight Control Systems. *International Journal of Aerospace Engineering*, 2015(672423), 2015. doi: 10.1155/2015/672423.

[17] Thomas E. Manning, Clifford L. Ratliff, and Edward J. Marquart. Bridging the Gap between Ground and Flight Tests - Virtual Flight Testing (VFT). In *Aircraft Engineering, Technology, and Operations Congress*, Los Angeles, USA, 1995. doi: 10.2514/6.1995-3875.

[18] Glenn Gebert, Joy Kelly, Juan Lopez, and Johnny Evers. Wind Tunnel Based Virtual Flight Testing. In *38th Aerospace Sciences Meeting & Exhibit*, Reno, USA, 2000. doi: 10.2514/6.2000-829.

[19] Rodney H. Rickets. Experimental Aeroelasticity - History, Status and Future in Brief. In *31st AIAA/ASME/ASCE/AHS/ASC Structures, Structural Dynamics and Materials Conference*, Long Beach, USA, 1990. doi: 10.2514/6.1990-978.

[20] Jewel B. Barlow, William H. Rae, Jr., and Alan Pope. *Low-Speed Wind Tunnel Testing*. John Wiley & Sons, 3rd edition, 1999. ISBN: 978-0-471-55774-6.

[21] Thomas G. Schmidt, Johannes Dillinger, Markus Ritter, Anna Altkuckatz, Charlotte Hanke, Marc Braune, Wolf R. Krüger, and Holger Mai. Design and Experimental Characterization of a Gust-Generator Concept with Rotating-Slotted Cylinders in the Low-Speed Wind Tunnel DNW-NWB. In *International Forum on Aeroelasticity and Structural Dynamics (IFASD 2024)*, Den Haag, The Netherlands, 2024. `https://elib.dlr.de/205804/`.

[22] Sergio Ricci, Francesco Toffol, A. De Gaspari, Luca Marchetti, Federico Fonte, Luca Riccobene, Paolo Mantegazza, John Berg, Eli Livne, and Kristi Morgansen. Wind Tunnel System for Active Flutter Suppression Research: Overview and Insights. *AIAA Journal*, 60(12):6692–6714, 2022. doi: 10.2514/1.J061985.

[23] Chester H. Wolowicz, J. Steven Brown, Jr., and William P. Gilbert. Similitude Requirements and Scaling Relationships as Applied to Model Testing. Technical Publication, TP-1435, NASA, 1979. https://ntrs.nasa.gov/citations/19790022005.

[24] Johannes Dillinger, Holger Mai, Wolf R. Krüger, Thomas G. Schmidt, and Felix Stalla. Design, Manufacturing and Identification of an Actively Controlled Flexible Wing for Subsonic Wind Tunnel Testing. In *International Forum on Aeroelasticity and Structural Dynamics (IFASD 2024)*, Den Haag, The Netherlands, 2024. https://elib.dlr.de/205840/.

[25] Bruce Owens, Jay Brandon, Mark Croom, Mike Fremaux, Gene Heim, and Dan Vicroy. Overview of Dynamic Test Techniques for Flight Dynamics Research at NASA LaRC. In *25th AIAA Aerodynamic Measurement Technology and Ground Testing Conference*, San Francisco, USA, 2006. doi: 10.2514/6.2006-3146.

[26] B. Krag. The Wind Tunnel Behaviour of a Scaled Model with a Gust Alleviation System in a Deterministic Gust Field. *Transactions of the Institute of Measurement and Control*, 1(3):141–153, 1979. doi: 10.1177/014233127900100303.

[27] Jurij Sodja and Roeland De Breuker. Design of an Increased-Fidelity Aeroelastic Experiment for Wing Response to Gust Excitation. In *AIAA SciTech 2022 Forum*, San Diago, USA, 2022. doi: 10.2514/6.2022-2418.

[28] Felix Stalla, Gertjan Looye, Manuel Pusch, and Spilios Theodoulis. Integrating Aeroelastic and Primary Flight Control: Robust Design and Wind Tunnel Demonstration. In *AIAA SciTech 2026 Forum*, Orlando, USA, 2026. AIAA. doi: 10.2514/6.2026-1557.

[29] Rudolf Brockhaus, Wolfgang Alles, and Robert Luckner. *Flugregelung*. Springer, 3rd edition, 2019. doi: 10.1007/978-3-642-01443-7.

[30] Martin R. Waszak and David K. Schmidt. Flight Dynamics of Aeroelastic Vehicles. *Journal of Aircraft*, 25(6):563–571, 1688. doi: 10.2514/3.45623.

[31] Christian Reschke. *Integrated Flight Loads Modelling and Analysis for Flexible Transport Aircraft*. Ph.D. thesis, University of Stuttgart, Stuttgart, Germany, 2006. doi: 10.18419/opus-3733.

[32] Thiemo Kier and Gertjan Looye. Unifying Manoeuvre and Gust Loads Analysis Models. In *International Forum on Aeroelasticity and Structural Dynamics (IFASD)*, Seattle, USA, 2009. https://elib.dlr.de/97798/.

[33] Bernard Etkin and Lloyd Duff Reid. *Dynamics of Flight: Stability and Control*. John Wiley & Sons, 3rd edition, 1995. ISBN: 978-0-471-03418-6.

[34] Felix Stalla, Thiemo M. Kier, Gertjan Looye, and Manuel Pusch. Aeroservoelastic Modeling and Robust Control for Gust Load Alleviation of an Experimental Wing. In *AIAA SciTech 2024 Forum*, Orlando, USA, 2024. AIAA. doi: 10.2514/6.2024-1442.

[35] J. Hofstee, T. Kier, C. Cerulli, and G. Looye. A Variable, Fully Flexible Dynamic Response Tool for Special Investigations (VarLoads). In *International Forum on Aeroelasticity and Structural Dynamics (IFASD)*, Amsterdam, Netherlands, 2003. https://elib.dlr.de/12206/.

[36] Thiemo M. Kier and Jeroen Hofstee. VarLoads - eine Simulationsumgebung zur Lastenberechnung eines voll flexiblen, freifliegenden Flugzeugs. In *Deutscher Luft- und Raumfahrtkongress (DLRK)*, Dresden, Germany, 2004. DGLR. https://elib.dlr.de/12207/.

[37] Fabian Grondman, Gertjan Looye, Richard O. Kuchar, Q. Ping Chu, and Erik-Jan Van Kampen. Design and Flight Testing of Incremental Nonlinear Dynamic Inversion-based Control Laws for a Passenger Aircraft. In *2018 AIAA Guidance, Navigation, and Control Conference*, Kissimmee, USA, 2018. AIAA. doi: 10.2514/6.2018-0385.

[38] Dale Enns, Dan Bugajski, Russ Hendrick, and Gunter Stein. Dynamic Inversion: an Evolving Methodology for Flight Control Design. *International Journal of Control*, 159(31):71–91, 1994. doi: 10.1080/00207179408923070.

[39] Thomas Lombaerts and Gertjan Looye. Design and Flight Testing of Manual Nonlinear Flight Control Laws. In *AIAA Guidance, Navigation, and Control Conference*, Portland, USA, 2011. AIAA. doi: 10.2514/6.2011-6469.

[40] Hans-Dieter Joos, Johann Bals, Gertjan Looye, Klaus Schnepper, and Andras Varga. A Multi-Objective Optimisation-Based Software Environment for Control Systems Design. In *Proceedings of the 2002 IEEE International Symposium on Computer Aided Control System Design*, Stockholm, Sweden, 2002. IEEE. doi: 10.1109/CACSD.2002.1036921.

[41] Twan Keijzer, Gertjan Looye, Q. Ping Chu, and Erik-Jan Van Kampen. Flight Testing of Incremental Backstepping based Control Laws with Angular Accelerometer Feedback. In *AIAA SciTech 2019 Forum*, San Diego, USA, 2019. AIAA. doi: 10.2514/6.2019-0129.

[42] Sigurd Skogestad and Ian Postlethwaite. *Multivariable Feedback Control*. John Wiley & Sons, Chichester, UK, 2nd edition edition, 2005. ISBN: 978-0-470-01168-3.

[43] John C. Doyle. Structured Uncertainty in Control System Design. In *24th IEEE Conference on Decision and Control*, pages 260–265, Fort Lauderdale, USA, 1985. doi: 10.1109/CDC.1985.268842.

[44] Peter M. Young. Controller Design with Mixed Uncertainties. In *Proceedings of the 1994 American Control Conference - ACC*, volume 2, pages 2333–2337, Fort Lauderdale, USA, 1994. doi: 10.1109/ACC.1994.752496.

[45] Gunter Stein and John C. Doyle. Beyond Singular Values and Loop Shapes. *Journal of Guidance*, 14(1), 1991. doi: 10.2514/3.20598.

[46] Gunter Stein. Respect the Unstable. *IEEE Control Systems Magazine*, 23(4):12–25, 2003. doi: 10.1109/MCS.2003.1213600.

[47] Thomas Schmidt et. al. Assessing Sensor-Model-Fusion Technologies on a Flexible Aeroelastic Wing Demonstrator through Wind Tunnel Testing in the DLR Project SAFER^2. In *German Aerospace Congress (DLRK)*, Augsburg, Germany, 2025. DGLR. `https://elib.dlr.de/217459/`.